

Large Eddy Simulation of a Vortex Ring Impacting a Bump

Heng Ren¹, Ning Zhao² and Xi-Yun Lu^{1,*}

¹ *Department of Modern Mechanics, University of Science and Technology of China, Hefei 230026, Anhui, China*

² *Department of Aerodynamics, Nanjing University of Aeronautics and Astronautics, Nanjing 210016, Jiangsu, China*

Received 10 July 2013; Accepted (in revised version) 27 September 2013

Available online 17 April 2014

Abstract. A vortex ring impacting a three-dimensional bump is studied using large eddy simulation for a Reynolds number $Re = 4 \times 10^4$ based on the initial diameter and translational speed of the vortex ring. The effects of bump height and vortex core thickness for thin and thick vortex rings on the vortical flow phenomena and the underlying physical mechanisms are investigated. Based on the analysis of the evolution of vortical structures, two typical kinds of vortical structures, i.e., the wrapping vortices and the hair-pin vortices, are identified and play an important role in the flow state evolution. The boundary vorticity flux is analyzed to reveal the mechanism of the vorticity generation on the bump surface. The circulation of the primary vortex ring reasonably elucidates some typical phases of flow evolution. Further, the analysis of turbulent kinetic energy reveals the transition from laminar to turbulent state. The results obtained in this study provide physical insight into the understanding of the mechanisms relevant to the flow evolution and the flow transition to turbulent state.

AMS subject classifications: 76F65, 76D17, 76F06

Key words: Large eddy simulation, vortex ring, vortical structure, turbulent state.

1 Introduction

As one of the typical forms of vortex motion, vortex rings widely exist in nature and engineering. The interaction of vortex rings with solid or fluid boundaries is a fundamental problem in fluid dynamics and has received considerable attention. This subject is also

*Corresponding author.

URL: <http://staff.ustc.edu.cn/~xlu/>

Email: renheng@mail.ustc.edu.cn (H. Ren), zhaoam@nuaa.edu.cn (N. Zhao), xlu@ustc.edu.cn (X. Y. Lu)

associated with a variety of practical applications, such as cavitated rings used for underwater drilling [1] and the downburst and aircraft interaction [2]. Moreover, the relevant physical flow behaviors and mechanisms are still unclear and are deserved to be studied.

Vortex ring interacting with a flat wall has been extensively studied [3–16]. These studies showed that as the primary vortex ring moves gradually toward the wall, its rate of approach slows down and its radius continues to increase. Meanwhile, the primary ring induces considerable secondary vorticity on the wall. When the Reynolds number of the ring is larger than 500 based on the initial diameter and translational speed of the vortex ring, the formation of the secondary ring occurs and then it interacts with the primary vortex ring. Actually, these studies are mainly restricted to relatively low Reynolds numbers, the highest Reynolds number in these studies is about 2840 [5]. Experimental study [5] has revealed that, beyond $Re = 3000$, the primary vortex ring will no longer remain stable as it approaches the wall. Thus, the instability and transition to turbulence for the vortex ring evolution should be considered when the Reynolds number becomes large enough.

Comparing with the numerous studies of vortex ring interacting with a flat wall, the investigation relevant to a vortex ring impacting a curved surface is scarce. Orlandi [17] numerically studied vortex pairs interacting with a two-dimensional circular cylinder with free-slip and no-slip boundary conditions. For the free-slip case, the dipole is observed to split into two vortices and then to rejoin on the cylinder. While for the no-slip interaction, the generation of dipolar and tripolar structures occurs on the cylinder surface. Verzicco et al. [18] further studied this problem. They found that the induced vortices become more apparent as the diameter of the cylinder increases. Allen et al. [19] presented experimental results of a vortex ring impinging on a moving sphere. They found that the secondary vorticity generated on the sphere surface leads to a decrease of the fluid impulse and an acceleration of the sphere. Recently, Sousa [20] studied a vortex ring impacting a stationary sphere for $Re = 1000$ using direct numerical simulation (DNS). After the secondary vortex ring is formed, they found its interaction with the primary ring results in the fast decay of circulation for the secondary ring.

For the vortex evolution with its transition to turbulence at large Reynolds number, large eddy simulation (LES) is a useful tool to study the flow behaviors from laminar to turbulent regime. Sreedhar and Ragab [21] used LES to investigate the response of longitudinal stationary vortices subjected to random perturbations and the subsequent transition to turbulence. The Reynolds number based on the core radius and maximum initial tangential velocity is 10^5 . Mansfield et al. [22] employed Lagrangian LES to investigate the collision of two coaxial vortex rings and successfully captured several distinctive phenomena observed experimentally [23]. Faddy and Pullin [24] numerically studied the flow structures of two counter-rotating vortices in three dimensions. They performed the simulations using DNS at low Reynolds number 10^3 and LES at high Reynolds number 2×10^4 , where the Reynolds number is based on the circulation of the Lamb-Oseen vortex.

In this paper, an LES technique is utilized to investigate the effects of bump height and vortex core thickness on the dynamics of vortical structures and the turbulent behaviors

when a vortex ring impacts a three-dimensional bump at Reynolds number $Re = 4 \times 10^4$. To our knowledge, the relevant work has never been performed before. The purpose of this work is to study the complex flow phenomena and the underlying mechanisms.

This paper is organized as follows. The mathematical formulation and numerical methods are presented in Section 2. The computational overview and validation are described in Section 3. Detailed results are then given in Section 4 and concluding remarks in Section 5.

2 Mathematical formulation and numerical methods

To investigate a vortex ring impinging on a bump, the three-dimensional Favre-filtered compressible Navier-Stokes (N-S) equations in generalized coordinates are employed. To non-dimensionalize the governing equations, the radius of the initial vortex ring and the far-field variables are used as characteristic quantities. It should be indicated that, similar to LES on the evolution of longitudinal stationary vortices [21,25], the present simulations are for a low Mach number of 0.3 based on the far-field speed of sound, which is very near the incompressible limit. Sreedhar and Ragab [21, 25] have verified that the approach based on the compressible N-S equations can reliably predict the incompressible flow characteristics of the vortex evolution.

The large eddy simulation is implemented for turbulence closure. In order to model some terms in the Favre-filtered equations arising from the unresolved scales, dynamic subgrid-scale (SGS) models for turbulent flows are employed. A detailed description of the mathematical formulation of the governing equations and the SGS models have been given in our previous papers [26,27].

The governing equations are numerically solved by a finite-volume method. As employed in our previous work [27, 29], the convective terms are discretized by a second-order central scheme and the viscous terms by a fourth-order centered scheme. Time advancement is performed by an implicit approximate-factorization method with sub-iterations to ensure a second-order accuracy. Moreover, the present numerical methods have already been used successfully to a variety of turbulent flows [26–29] and have been verified to provide the reliable calculations.

3 Computational overview and validation

3.1 Computation overview

According to the schematic as depicted in Fig. 1, a vortex ring with radius R_0 is initially placed at $x_c = (0,0,H_v)$, where H_v is the distance between the vortex ring center and the bottom wall. The bump has a circular base with a cosine-squared cross section which is defined as

$$z(x,y) = H_b \cos^2\left(\frac{\pi\sqrt{x^2+y^2}}{6}\right), \quad (3.1)$$

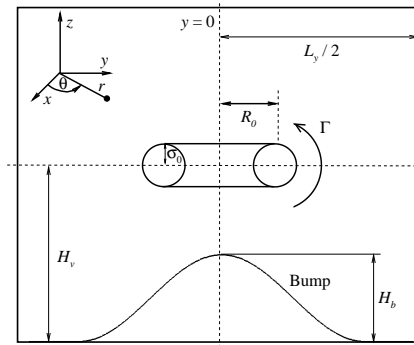


Figure 1: Schematic diagram of a vortex ring approaching a bump.

where H_b is the bump height. The vortex core is initiated by a Gaussian vorticity distribution [30]

$$\omega_\theta = \frac{\Gamma_0}{\pi\sigma_0^2} e^{(-s^2/\sigma_0^2)}, \quad (3.2)$$

where s is the radial distance from the center of the core, σ_0 is the initial core radius, and Γ_0 is the initial circulation of the vortex ring. The initial translational speed of the vortex ring can be represented as [31]

$$u_s = \frac{\Gamma_0}{4\pi R_0} \left(\ln \frac{8R_0}{\sigma_0} - \frac{1}{4} \right). \quad (3.3)$$

To deal with the instability of the vortex ring, an azimuthal disturbance is introduced by imposing a radial displacement on the axis of the ring and the local radius $R(\theta)$ is then expressed as [32]

$$R(\theta) = R_0 [1 + \zeta g(\theta)], \quad (3.4a)$$

$$g(\theta) = \sum_{n=1}^{32} A_n \sin(n\theta) + B_n \cos(n\theta), \quad (3.4b)$$

where ζ is a small parameter and is chosen as 2×10^{-4} [32, 33].

In the computation, the effects of bump height and vortex core thickness are investigated. The parameters of six cases are given in Table 1. For all the cases, the bump base diameter is held constant with $6R_0$ and the height H_b/R_0 varies from 1.8 to 3.0. The initial translation speed of the vortex ring is $u_s = 0.3$ and the Reynolds number, based on the translational speed and the ring diameter, is $Re = 4 \times 10^4$. For the thin vortex ring (cases 1-3), we have the slenderness ratio $\sigma_0/R_0 = 0.2$ and the Reynolds number based on the circulation of vortex ring $Re_\Gamma = 7.31 \times 10^4$. For the thick vortex ring (cases 4-6), $\sigma_0/R_0 = 0.4$ and $Re_\Gamma = 9.15 \times 10^4$. The computational domain extends for $16R_0$ in the x and y directions and $12R_0$ in the z or vertical direction, i.e., $L_x/R_0 = L_y/R_0 = 16$, $L_z/R_0 = 12$. The grid-spacing is uniform in the x and y directions, and a grid stretching in the z direction

Table 1: Computational parameters. The * superscript denotes quantities at time $T=5$.

Case	σ_0/R_0	H_b/R_0	Re_Γ	t_1	Γ^*/Γ_0	R^*/R_0	σ^*/R_0
1	0.2	1.8	7.31×10^4	10	0.986	1.024	0.216
2	0.2	2.4	7.31×10^4	10	0.985	1.018	0.220
3	0.2	3.0	7.31×10^4	10	0.989	1.021	0.218
4	0.4	1.8	9.15×10^4	15	0.983	1.016	0.419
5	0.4	2.4	9.15×10^4	15	0.986	1.019	0.421
6	0.4	3.0	9.15×10^4	15	0.982	1.020	0.417

is used to increase the grid resolution near the surface. Periodic boundary conditions are employed in the x and y directions. No-slip boundary condition is used on the bump surface and a far-field boundary condition is applied in the $z=L_z$ plane.

To prevent the perturbation to be extremely weak as the vortex ring collides with the bump, the vortex ring should be placed at a large height over the bump. This should excessively increase the amount of computation. Following the treatment by evolving the vortex ring in a precursor simulation [34], after the thin vortex ring has evolved for time $t_1 = 10$ and the thick vortex ring for $t_1 = 15$, it is obtained that the perturbation energy for both the rings reaches 1.5×10^{-4} approximately. Then the obtained velocity field is interpolated at $H_v = 6R_0$ to prescribe the initial velocity field for the vortex-bump interaction simulation. To examine the reliability of this treatment, Table 1 lists the quantities of the evolved vortex rings at time $T=5$, where T is defined as $T = t - t_1$ and non-dimensionalized by R_0^2/Γ_0 ; it is identified that the quantities are reasonably consistent with the initial parameters.

To clearly present the post-processing, an averaging operation will be needed based on the time-dependent resolved density $\bar{\rho}$, pressure \bar{p} and velocity \bar{u}_i obtained in the LES. The symbol $\langle \rangle$ used in this paper represents the average in the azimuthal direction after transforming the data from the Cartesian coordinate system (x, y, z) into the cylindrical coordinate (r, θ, z) as shown in Fig. 1.

3.2 Validation

Our code is validated in terms of a vortex ring interacting with a flat wall at $\text{Re} = 830$, which has been studied by Chu et al. [9] and Cheng et al. [15]. The initial height of the vortex ring is $H_v = 3R_0$ and a grid resolution $R_0 = 30\Delta x$ is used for the simulation [15]. As depicted in Fig. 2, the vorticity pattern in the $y=0$ plane is compared with the experimental observation of Chu et al. [9]. The essential flow features are accurately reproduced in our simulation, including the primary and secondary vortex rings interaction and the formation of the tertiary ring. The trajectory of the primary ring center is also compared with the previous results in Fig. 3. It can be seen that our results agree well with the experimental data [9] and numerical results [15].

Further, to assess the effect of grid resolution on the calculated results for the present problem, three test cases for case 1 have been examined with the parameters in Table 2.

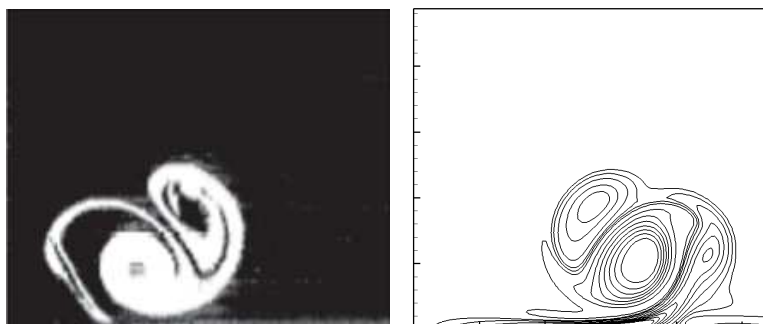


Figure 2: Vorticity pattern for the interaction of vortex ring and flat wall by experimental observation [9] (left panel) and the present numerical result (right panel).

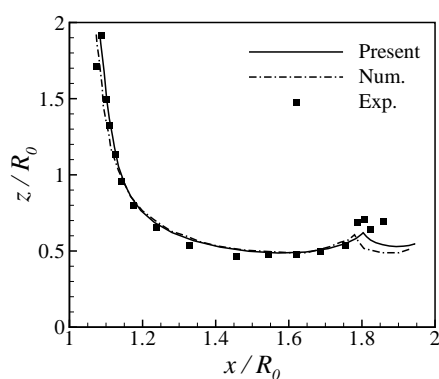


Figure 3: Trajectory of the primary ring center at $Re = 830$. The solid and dashdot lines denote the numerical results by the present simulation and by Cheng et al. [15], respectively. The symbols represent the experimental data of Chu et al. [9].

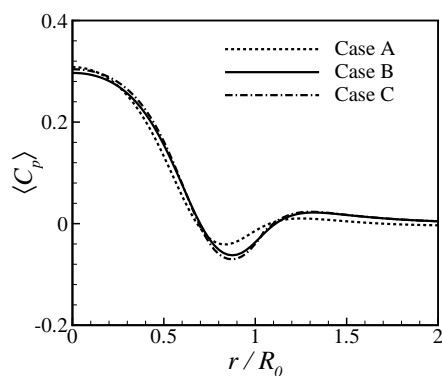


Figure 4: Comparison of azimuthally averaged pressure coefficients on the bump surface for three test cases at $T = 15.0$.

For all the test cases the minimum grid spacing in the z direction is $\Delta z_{\min} = 2 \times 10^{-5} R_0$. Fig. 4 shows the distributions of the azimuthally averaged pressure coefficient defined by $\langle C_p \rangle = R_0^2 (\langle \bar{p} \rangle - p_\infty) / (\langle \bar{\rho} \rangle \Gamma_0^2)$ along the radial direction, where p_∞ represents the far-field

Table 2: Comparison of the calculated results with different grid resolutions for case 1 at $T=15.0$. Here, N_x , N_y , and N_z represent the grid number in the x , y and z directions, respectively. $|\omega|_{\max}$ and E denote the maximum vorticity magnitude on the surface and the total kinetic energy in the flow field, respectively.

Case	$N_x \times N_y \times N_z$	R_0	$ \omega _{\max}$	E
A	$481 \times 481 \times 241$	$30\Delta x$	114.4	1.0018
B	$641 \times 641 \times 321$	$40\Delta x$	123.6	1.0625
C	$801 \times 801 \times 401$	$50\Delta x$	126.1	1.0704

pressure. The instant $T = 15.0$ in Table 2 and Fig. 4 corresponds to the vortex ring close to the bump with boundary layer separation which is sensitive to the grid resolutions. As shown in Fig. 4, the results for the test cases B and C collapse together, indicating a reasonable convergence for the grid resolution. Moreover, the differences of the relevant parameters listed in Table 2 for cases B and C are small. Thus the $641 \times 641 \times 321$ grid with resolution $R_0 = 40\Delta x$ can accurately predict the flow characteristics and is used in the present simulation.

4 Results and discussion

4.1 Vortical structures

The flow field of a vortex ring impacting a bump involves an array of complicated flow phenomena, such as the generation and deformation of secondary vortex ring, the interaction of vortex rings, and the instability and breakdown of vortex rings. To assess the existence of vortical structures in the flow field, these phenomena are analyzed here for different bump heights and vortex core thicknesses with the cases given in Table 1.

The evolutions of vortical structures are shown in Fig. 5 for the thin vortex ring with different bump heights (i.e., cases 1-3). Here, the vortical structures are depicted by iso-surface of the Q criterion [35], described as $Q = -(\|\mathbf{S}\|^2 - \|\mathbf{\Omega}\|^2)/2$, where \mathbf{S} and $\mathbf{\Omega}$ denote the strain and the rotation tensor, respectively. A positive value of Q presents the regions in which the rotation exceeds the strain. Thus, the instantaneous vortical structures depicted by $Q=0.5$ are illustrated here. For comparability of the vortical structures for cases 1-3 as shown in Fig. 5, it is indicated that the distances between the vortex ring center and the bump top are $0.32R_0$ approximately for case 1 at $T = 15.0$, case 2 at $T = 12.5$, and case 3 at $T = 10.0$.

From Fig. 5(a) for case 1, when the primary vortex ring moves close to the bump, a vorticity layer is obviously generated on the core surface of bump at $T = 15.0$. Then the separation of boundary layer occurs in the adverse pressure gradient region resulting in the generation of secondary vortex ring at $T = 17.5$. Due to the growth of the azimuthal perturbation, the primary vortex ring develops into a wavy-like structure at $T = 17.5$ and 20.0 . Furthermore, by means of Fourier analysis of the azimuthal perturbation, it is identified that the wave number of the most unstable mode for the primary ring is $k = 11$, consistent with the theoretical estimate of the dominant mode $k = 2.26/\sigma_0$ approximately

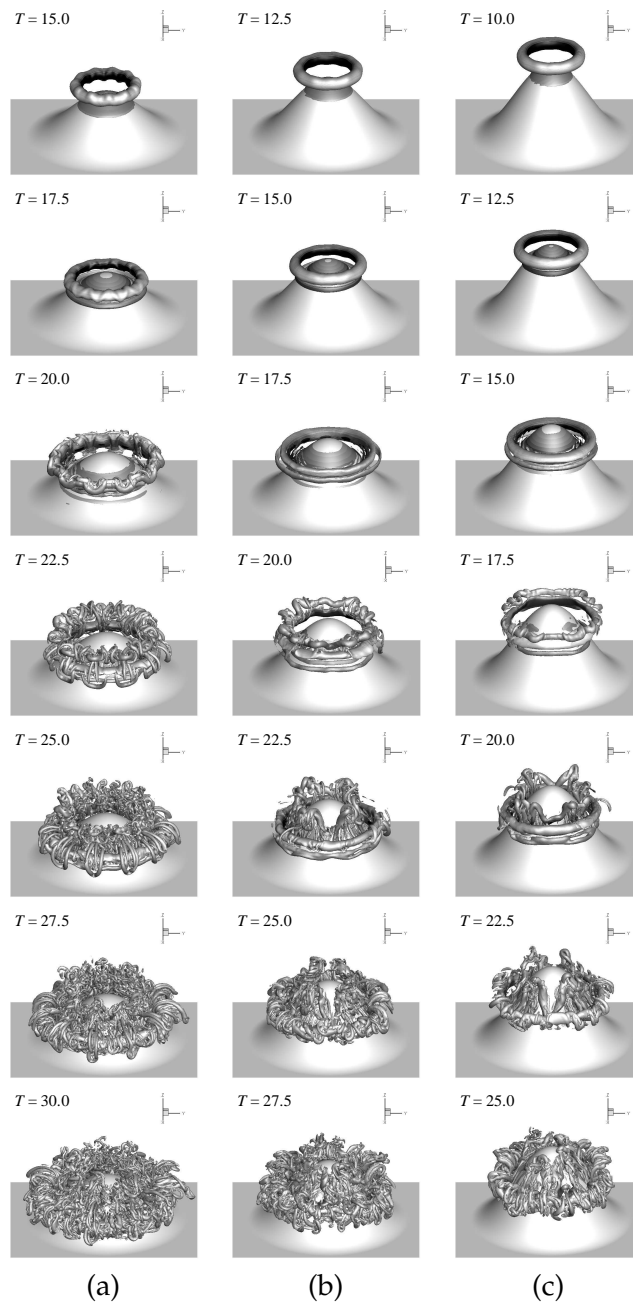


Figure 5: Evolution of vortical structures visualized by an isosurface of the Q criterion with $Q=0.5$ for thin vortex rings: (a) case 1 (left column), (b) case 2 (middle column), (c) case 3 (right column).

by Maxworthy [36] and the number of the wavy-like structures observed at $T=17.5$ and 20.0 . Further, after the primary ring collides with the bump surface, the secondary ring generated lifts up from the surface and then moves over the primary vortex ring. The

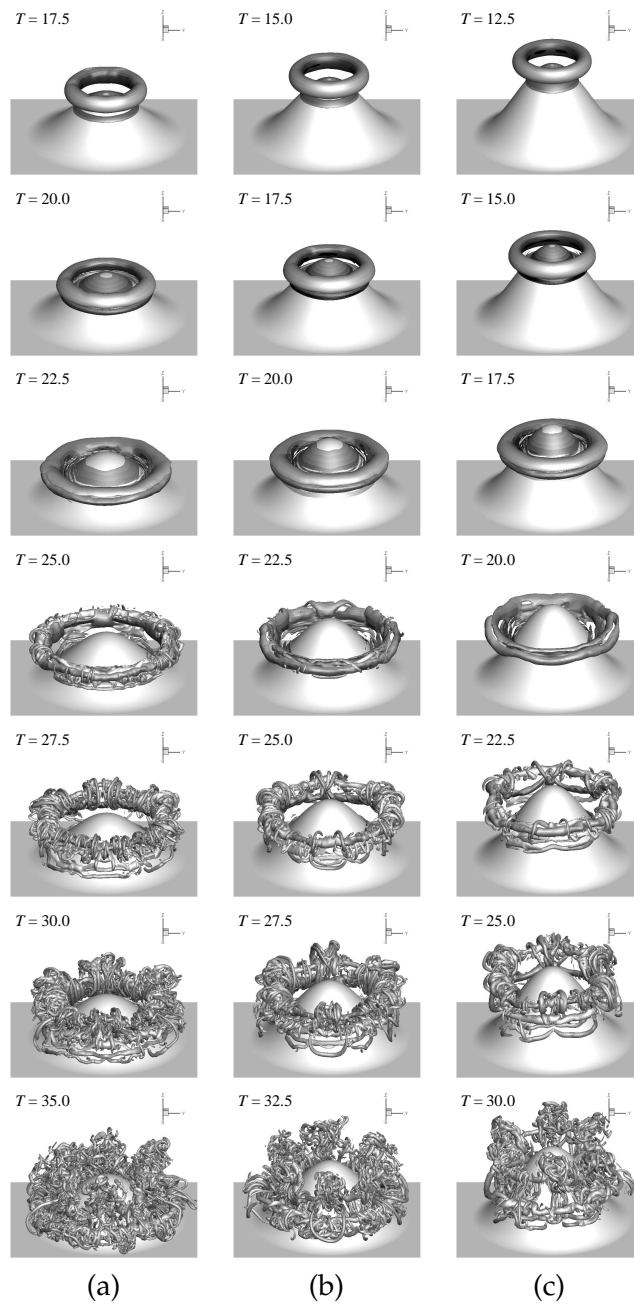


Figure 6: Evolution of vortical structures visualized by isosurface of the Q criterion with $Q=0.5$ for thick vortex rings: (a) case 4 (left column), (b) case 5 (middle column), (c) case 6 (right column).

interaction of the primary and secondary rings decelerates the radial expansion of the primary ring and causes it to rebound from the surface. Then, the secondary ring has already moved up the primary ring at $T = 22.5$. During the evolution of the secondary

ring, it is reasonably obtained that the wave number of the most unstable mode for the secondary ring is also $k = 11$. Subsequently, a variety of loop-like vortices wrapping around both the primary and secondary vortex rings (briefly called "wrapping vortices") are formed at $T = 25.0$ and 27.5 . The generation of these wrapping vortices is associated with a short-wavelength instability of the vortex rings [32]. Finally, the complicated interactions of the wrapping vortices and vortex rings over the bump surface result in the breakdown of the vortical structures into small-scale vortices, say at $T = 30.0$ in Fig. 5(a), and further lead to the vortical flow transition to turbulent state which will be analyzed below.

To investigate the effect of the bump height on the flow structures, Figs. 5(b) and 5(c) show the vortical structures for cases 2 and 3, respectively. The evolution of vortical structures for the generation of secondary vortex ring is similar to case 1. When the wavy-like secondary ring moves up the primary ring, the secondary ring stretches significantly and causes severe distortion of the secondary ring at $T = 20.0$ for case 2 in Fig. 5(b) and $T = 17.5$ for case 3 in Fig. 5(c). Then, the intense stretching effect results in the disconnection of the secondary ring and the generation of 'hair-pin vortices' at $T = 22.5$ for case 2 and $T = 20.0$ for case 3. These hair-pin vortices evolve over the bump surface because of the induction of the primary vortex ring. When the hair-pin vortices collide with the surface, the vortices break into small-scale ones and move upwards over the bump surface at $T = 25.0$ for case 2 and $T = 22.5$ for case 3. Subsequently, the interactions of the hair-pin vortices and vortex rings over the bump surface result in the transition from laminar to turbulent state.

From the preceding description of the interaction and evolution of vortices for the thin vortex ring impacting the bump, it is identified that two typical kinds of vortical structures, i.e., the wrapping vortices and the hair-pin vortices. To reveal the effect of the bump height on the flow evolution, we have reasonably obtained that the wrapping vortices play an important role in the flow state evolution for case 1, and the hair-pin vortices act as a dominant role for cases 2 and 3.

Further, Fig. 6 shows the evolutions of vortical structures for the thick vortex ring with different bump heights. Similarly, for comparability of the vortical structures for cases 4-6, the distances between the vortex ring center and the bump top are $0.21R_0$ approximately for case 4 at $T = 17.5$, case 5 at $T = 15.0$, and case 6 at $T = 12.5$. From Fig. 6(a) for case 4, as the primary vortex ring approaches the bump, a secondary vortex ring is gradually generated at $T = 20.0$ and 22.5 . Then, the secondary vortex ring evolves upwards and interacts with the primary one at $T = 25.0$. When the secondary ring locates over the primary ring, some loop-like vortices [37,38] wrapping around both the primary and secondary rings occur obviously at $T = 27.5$ and also strengthen gradually at $T = 30.0$. Furthermore, the evolution of vortical structures becomes more complicated, such as the flow structures at $T = 35.0$, and accompanies with the breakdown of vortices and the flow transition to turbulent state.

To analyze the effect of the bump height on the flow structures for the thick vortex ring, Figs. 6(b) and 6(c) also show the vortical structures for cases 5 and 6, respectively. It

is noticed that the evolutions of vortical structures for cases 4-6 are qualitatively similar. However, with the increase of the bump height (i.e., from case 4 to 6), it is observed that the number of loop-like vortices wrapping around both the primary and secondary rings obviously reduces, such as the flow patterns at $T=30.0$ for case 4, $T=27.5$ for case 5, and $T=25.0$ for case 6. This character is also confirmed in subsection 4.4 based on the analysis of the total enstrophy of the wrapping vortices.

4.2 Pressure and boundary vorticity flux on the surface

As the vortex ring impacts the bump, the generation of vorticity on the bump surface is an important process to affect the overall flow characteristics. The mechanisms relevant to the evolution of vortical structures demonstrated above are further analyzed from the body surface. A quantitative understanding of the vorticity generation on the surface is of fundamental significance and may improve our capability for flow analysis. The boundary vorticity flux (BVF) represents an on-surface dynamic process which causes the formation of vortical structures and is also related to the pressure gradient on the surface [39].

Fig. 7 shows the distributions of azimuthally averaged pressure coefficient along the radial direction for case 1. As the vortex ring is approaching the bump, the pressure distribution on the bump core region increases gradually such as from $T=12.5$ to 15.0 . It is seen that the negative pressure coefficient on the vortex ring impacting region occurs at $T=15.0$. Then, as the secondary vortex ring is generated at $T=17.5$ as shown in Fig. 5(a), the negative pressure coefficient becomes more obvious and the pressure distribution over the bump core region reduces gradually. Subsequently, after the vortex ring collides with the bump, the pressure distribution varies smoothly, such as at $T=22.5$ and 25.0 in Fig. 7.

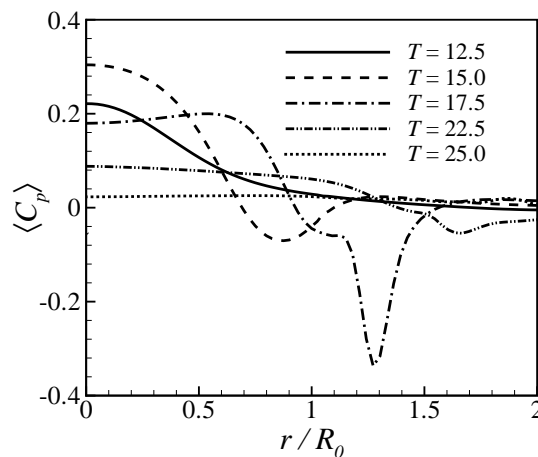


Figure 7: Azimuthally averaged pressure coefficient on the bump surface for case 1.

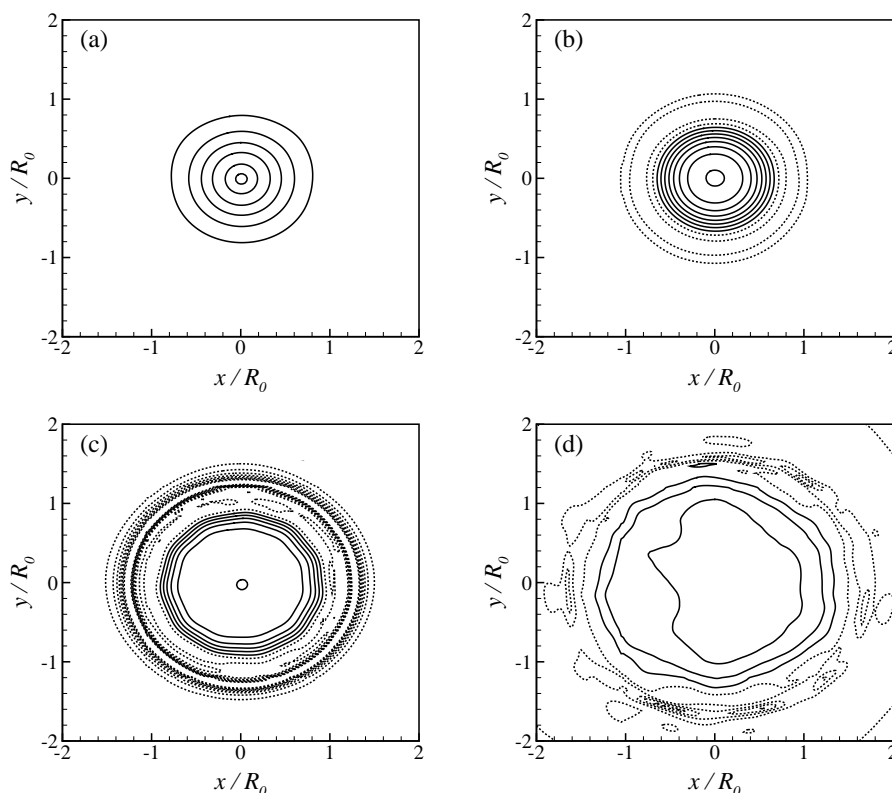


Figure 8: Contours of the pressure coefficient on the bump surface for case 1. (a) $T = 12.5$, (b) 15.0, (c) 17.5, (d) 22.5. Here, solid and dashed lines denote positive and negative values, respectively. The contour increment is $\Delta C_p = 0.04$ with $|C_p| \leq 0.3$.

To clearly demonstrate the pressure distribution on the bump, Fig. 8 shows the pressure contours on the surface. It is seen that the contours of the pressure coefficient are smooth distribution in the azimuthal direction at $T = 12.5$ and 15.0. Moreover, the region with negative distribution at $T = 15.0$ is related to the vortex ring impacting on the bump surface. Then, the contours become the wave-like azimuthal distribution at $T = 17.5$, which is reasonably related to the wavy-like structure of the primary vortex ring caused by the azimuthal instability as exhibited in Fig. 5(a). Furthermore, the contours of the negative pressure coefficient at $T = 22.5$ present some local patterns along the azimuthal direction, corresponding to the loop-like vortices wrapping around both the primary and secondary vortex rings.

Further, for the present flow with a high Reynolds number, the BVF can be approximately written as [27, 39] $\sigma_\omega = \nu \partial \omega / \partial n \simeq \mathbf{n} \times \nabla \bar{p} / \bar{\rho}$, where ν is the kinematic viscosity, and \mathbf{n} is the normal unit vector on a solid wall. This relation is reasonably examined based on the present calculated data. Thus, we can learn that the BVF is in turn dominated by the tangent pressure gradient on the surface, which also becomes a cause of

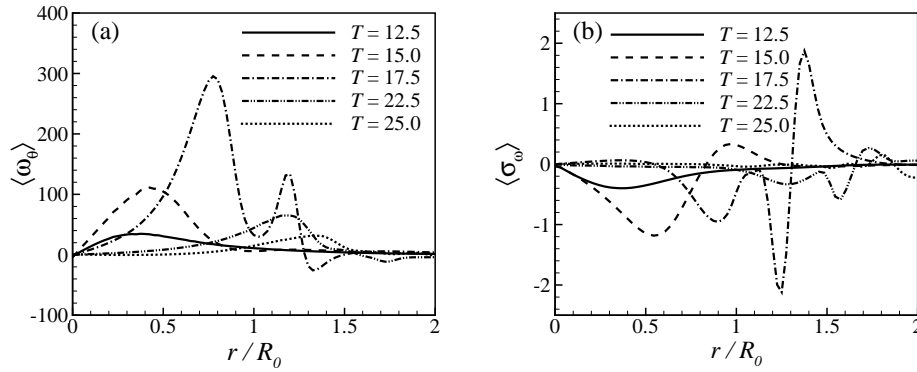


Figure 9: Azimuthally averaged (a) vorticity $\langle \omega_\theta \rangle$ and (b) BVF $\langle \sigma_\omega \rangle$ on the surface for case 1.

new vorticity [39]. To analyze the vorticity and the BVF, Fig. 9 shows the distributions of azimuthally averaged vorticity component $\langle \omega_\theta \rangle$ and BVF $\langle \sigma_\omega \rangle$ on the bump surface for case 1. It can be seen that both the magnitudes of $\langle \omega_\theta \rangle$ and $\langle \sigma_\omega \rangle$ increase rapidly as the primary vortex ring moves close to the bump. At $T = 17.5$, the magnitudes reach a relatively high value. Subsequently, the magnitudes decrease gradually, indicating that the generation of vorticity from the bump surface becomes weak.

The distributions of $\langle \omega_\theta \rangle$ and $\langle \sigma_\omega \rangle$ on the bump surface for all the cases are shown in Fig. 10. For comparison, we choose approximately the instant when the secondary ring is formed. The corresponding distance between the bump top and the vortex ring center is approximately $0.20R_0$ for cases 1-3 and $0.24R_0$ for cases 4-6. It is seen that the magnitudes of $\langle \omega_\theta \rangle$ and $\langle \sigma_\omega \rangle$ on the bump surface decrease for both the thin and thick vortex rings as the bump height increases, i.e., from case 1 to 3 for the thin ring and from case 4 to 6 for the thick ring. This suggests that the vorticity generation capacity on the bump surface decreases with the increase of the bump height.

4.3 Circulation and kinetic energy

To investigate the global behavior of flow evolution, we further analyze the circulation of the primary vortex ring and the total kinetic energy in the flow field. Here, the circulation of vortex ring is calculated by [32]

$$\Gamma = \int \langle \omega_\theta \rangle dr dz, \tag{4.1}$$

where the integration domain for the primary vortex ring is chosen as the region with $\langle \omega_\theta \rangle < 0$ [30]. Furthermore, the total kinetic energy in the flow field is defined as

$$E = \frac{1}{2} \int (\bar{\mathbf{u}} \cdot \bar{\mathbf{u}}) dV, \tag{4.2}$$

where $\bar{\mathbf{u}}$ represents the resolved velocity and the integral domain is the whole flow field.

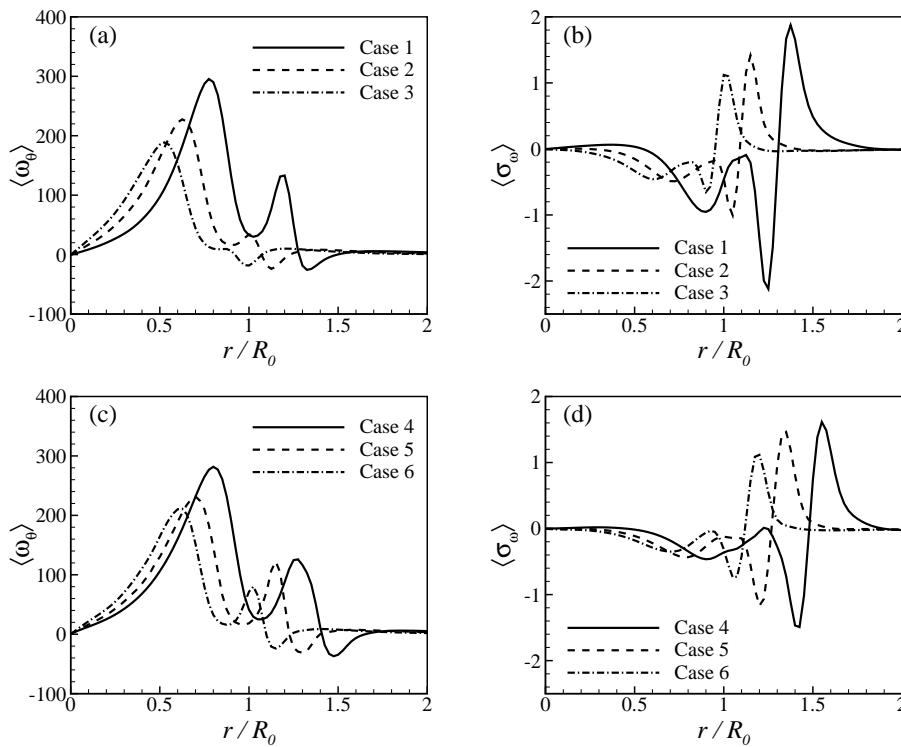


Figure 10: Azimuthally averaged (a,c) vorticity $\langle \omega_\theta \rangle$ and (b,d) BVF $\langle \sigma_\omega \rangle$ on the surface when the distance between the bump top and the vortex ring center is approximately $0.20R_0$ for cases 1-3 and $0.24R_0$ for cases 4-6. Correspondingly, case 1: $T=17.5$; case 2: $T=15.0$; case 3: $T=12.5$, case 4: $T=20.0$; case 5: $T=17.5$; case 6: $T=15.0$.

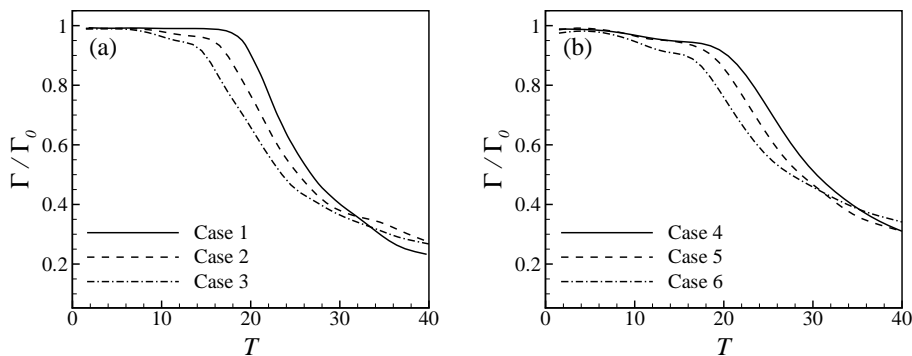


Figure 11: Evolution of the circulation for the primary vortex ring: (a) cases 1-3, (b) cases 4-6.

The circulation of the primary vortex ring is shown in Fig. 11. Based on the profiles for all the cases, the evolution of circulation can be divided into three phases. Firstly, as the vortex ring is away from the bump, the circulation is nearly constant. Then the collision

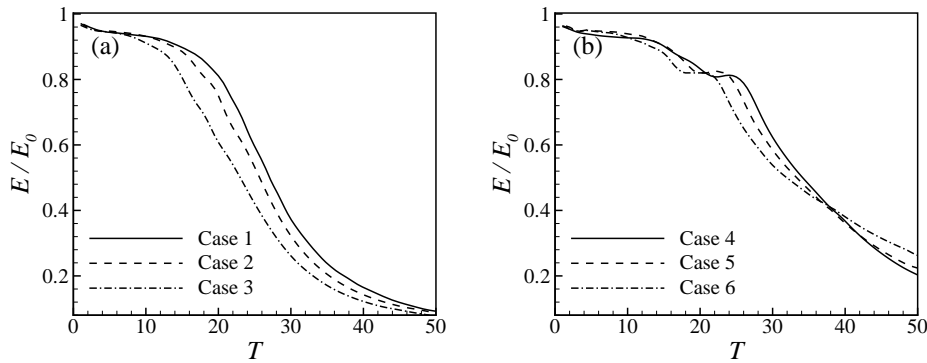


Figure 12: Evolution of the total kinetic energy in the flow field: (a) cases 1-3, (b) cases 4-6.

of the vortex ring with the bump occurs and the circulation decreases quickly. Thirdly, after the vortices break up into small-scale ones, the strength of vortex ring becomes relatively weak and the circulation decreases slowly. As the bump height increases, the decay rate of circulation decreases for both the thin and thick vortex rings, as depicted in Figs. 11(a) and 11(b). This behavior is attributed to a weaker interaction between the primary vortex ring and the surface when H_b increases.

Further, Fig. 12 shows the evolution of total kinetic energy normalized by the initial kinetic energy E_0 . It is seen from Fig. 12(a) for the thin vortex ring that the kinetic energy decreases slowly due to viscous dissipation before the vortex ring collides with the bump surface. Then the kinetic energy decreases quickly as the vortex-surface interaction. With the increase of the bump height, the decay rate of the kinetic energy becomes smaller, consistent with the evolution of circulation shown in Fig. 11. Moreover, the total kinetic energy for the thick vortex ring is shown in Fig. 12(b) and decays slowly compared with the thin ring in Fig. 12(a), indicating that the thin vortex ring evolves more rapidly than the thick ring.

4.4 Flow behavior in turbulent state

Based on the preceding discussion, after the vortical structures break into small-scale vortices, the transition from laminar to turbulent state occurs. To investigate the flow evolution and the relevant turbulent behavior, we analyze the turbulent kinetic energy (TKE), which is defined as

$$\text{TKE} = \frac{1}{2} \int (\mathbf{u}' \cdot \mathbf{u}') dV, \tag{4.3}$$

where \mathbf{u}' represents the velocity fluctuations and is defined as $\mathbf{u}' = \bar{\mathbf{u}} - \langle \bar{\mathbf{u}} \rangle$, and the integral domain is the whole flow field.

Fig. 13 shows the evolution of TKE. Before the vortex ring interacts with the bump, the turbulent kinetic energy vanishes, corresponding to laminar flow state. As a typical example, we mainly discuss the behavior for case 1. It is identified that the generation of

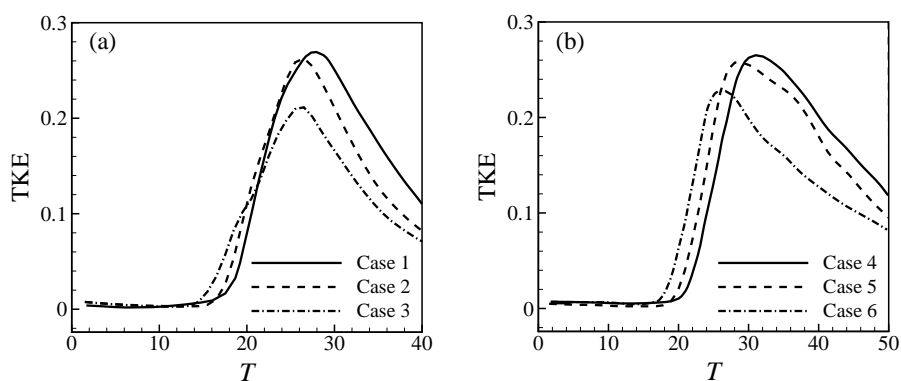


Figure 13: Evolution of turbulent kinetic energy integrated over the whole domain: (a) cases 1-3, (b) cases 4-6.

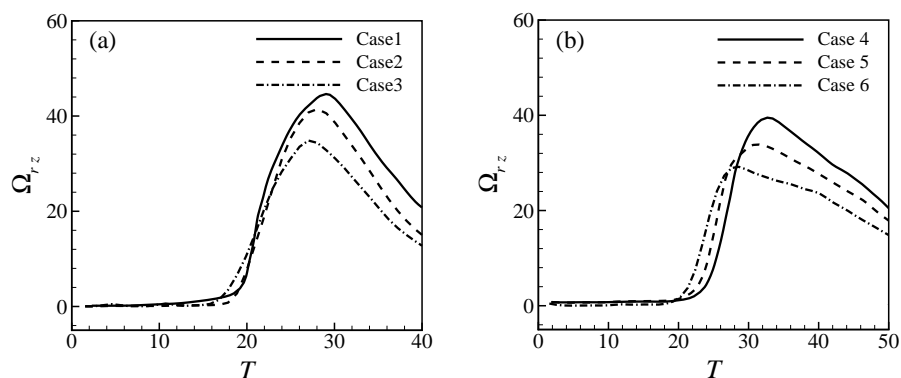


Figure 14: Evolution of the enstrophy of wrapping and hair-pin vortices integrated over the whole domain: (a) cases 1-3, (b) cases 4-6.

secondary vortex ring at $T = 17.5$ approximately is an indication of the growth of TKE. Then with the development of the azimuthal instability in the vortical structures and the breakdown of these vortices, the TKE grows rapidly and reaches its maximum at approximately $T = 28$, representing the flow transition to turbulence [21, 25]. After $T = 28$, the TKE decays quickly due to the vortical evolution and viscous decay. Moreover, compared with cases 1-3, as the bump height increases, the maximum of TKE decreases gradually in Fig. 13(a). Further, as shown in Fig. 13(b) for the thick vortex ring, the behavior of TKE and its evolution for cases 4-6 are similar to cases 1-3 for the thin vortex ring.

According to the investigation of an isolated vortex ring transition from the laminar to the turbulent state by Archer et al. [32], the shedding of hair-pin vortices along the azimuthal direction of the ring indicates turbulent flow state. In this study, two typical vortical structures, i.e., the wrapping vortices and hair-pin vortices, are identified, which play a similar role in the occurrence of turbulent flow state. As both the wrapping and

hair-pin vortices are mainly distributed by the vorticity components in the radial and vertical directions, we can reasonably measure the strength of these vortices by integrating the enstrophy in the whole flow field,

$$\Omega_{rz} = \frac{1}{2} \int (\omega_r^2 + \omega_z^2) dV, \quad (4.4)$$

where ω_r and ω_z represent the vorticity components in the radial and vertical directions, respectively.

The evolution of Ω_{rz} is shown in Fig. 14. Compared with the profiles of TKE in Fig. 13, it is interesting to notice that the time-dependent characters of both Ω_{rz} and TKE exhibit the similar manner. The generation of Ω_{rz} (or the wrapping vortices and hair-pin vortices) corresponds to the instant of the growth of TKE. This behavior reasonably indicates that the formation of the wrapping and hair-pin vortices plays an important role in the flow transition from laminar to turbulent state.

5 Concluding remarks

The interaction between a vortex ring and a three-dimensional bump has been studied by means of an LES technique. The effects of bump height and vortex core thickness for thin and thick vortex rings on the vortical flow phenomena and the underlying physical mechanisms were investigated and are summarized briefly as follows.

As a vortex ring impinges on a bump, we have analyzed the evolution of vortical structures and demonstrated an array of vortical flow phenomena, such as the generation and deformation of secondary vortex ring, the interaction of vortex rings, and the instability and breakdown of vortex rings. For the thin vortex ring impacting the bump, two typical kinds of vortical structures are identified and briefly represented as the wrapping vortices and the hair-pin vortices, corresponding to lower bump height and higher bump height. For the thick vortex ring impacting the bump, the similar evolution of vortical structures with several bump heights occurs and the wrapping vortices are generated. Further, it is found that the wrapping vortices and the hair-pin vortices play an important role in the flow state evolution.

The vorticity generation on the bump surface is an important process to affect the overall flow characteristics. The relevant mechanism is analyzed from the body surface in terms of the BVF and pressure gradient on the surface. It is noticed that the generation of secondary vortex ring reasonably corresponds to large BVF, and subsequently the vorticity generation from the bump surface becomes weak based on the variation of BVF. Moreover, the vorticity generation capacity on the bump surface decreases with the increase of the bump height for both the thin and thick vortex rings.

The circulation of the primary vortex ring and the total kinetic energy in the flow field have been investigated to reveal the global behavior of flow evolution. The evolution of circulation can be divided into three phases. Firstly, as the vortex ring is far away from

the bump, the circulation is nearly constant. Then the collision of the vortex ring with the bump occurs and the circulation decreases quickly. Thirdly, after the vortices break up into small-scale ones, the circulation decreases slowly. Moreover, the total kinetic energy decreases slowly due to viscous dissipation before the vortex ring collides with the bump surface, and then decreases quickly as the vortex-surface interaction.

After the vortical structures break into small-scale vortices, the transition from laminar to turbulent state occurs and the evolution of TKE has been analyzed. Before the vortex ring interacts with the bump, the TKE vanishes, corresponding to laminar flow state. Then with the development of the azimuthal instability in the vortical structures and the breakdown of these vortices, the TKE grows rapidly and reaches its maximum, representing the flow transition to turbulence. Subsequently, the TKE decays quickly due to the vortical evolution and viscous decay. Further, the enstrophy of the wrapping vortices and hair-pin vortices is investigated. It is found that the formation of the wrapping and hair-pin vortices plays an important role in the flow transition from laminar to turbulent state.

Acknowledgments

This work was supported by the National Natural Science Foundation of China (Grants 11132010, 11372304 and 11072236) and the 111 Project (Grant B07033).

References

- [1] G. L. CHAHINE AND P. F. GENOUX, *Collapse of a cavitating vortex ring*, J. Fluid Eng., 105 (1983), pp. 400–405.
- [2] T. S. LUNDGREN AND N. N. MANSOUR, *Vortex ring bubbles*, J. Fluid Mech., 224 (1991), pp. 177–196.
- [3] U. BOLDES AND J. C. FERRERI, *Behavior of vortex rings in the vicinity of a wall*, Phys. Fluids, 16 (1973), pp. 2005–2006.
- [4] H. YAMADA, O. MOCHIZUKI, H. YAMABE AND T. MATSUI, *Pressure variation on a flat wall induced by an approaching vortex ring*, J. Phys. Soc. Japan, 54 (1985), pp. 4151–4160.
- [5] J. D. A. WALKER, C. R. SMITH, A. W. CERRA AND T. L. DOLIGALSKI, *The impact of a vortex ring on a wall*, J. Fluid Mech., 181 (1987), pp. 99–140.
- [6] C. C. CHU, C. T. WANG AND C. C. CHANG, *A vortex ring impinging on a solid plane surface—vortex structure and surface force*, Phys. Fluids, 7 (1995), pp. 1391–1401.
- [7] P. ORLANDI, *Vortex dipole rebound from a wall*, Phys. Fluids A, 2 (1990), pp. 1429–1436.
- [8] P. ORLANDI AND R. VERZICCO, *Vortex rings impinging on walls: axisymmetric and three-dimensional simulations*, J. Fluid Mech., 256 (1993), pp. 615–646.
- [9] C. C. CHU, C. T. WANG AND C. S. HSIEH, *An experimental investigation of vortex motions near surfaces*, Phys. Fluids A, 5 (1993), pp. 662–676.
- [10] C. C. CHANG, *Potential flow and forces for incompressible viscous flow*, Proc. R. Soc. Lond. A, 437 (1992), pp. 517–525.

- [11] D. FABRIS, D. LIEPMANN AND D. MARCUS, *Quantitative experimental and numerical investigation of a vortex ring impinging on a wall*, Phys. Fluids, 8 (1996), pp. 2640–2649.
- [12] T. T. LIM, T. B. NICKELS AND M. S. CHONG, *A note on the cause of rebound in the head-on collision of a vortex ring with a wall*, Exp. Fluids, 12 (1991), pp. 41–48.
- [13] J. D. SWEARINGEN, J. D. CROUCH AND R. A. HANDLER, *Dynamics and stability of a vortex ring impacting a solid boundary*, J. Fluid Mech., 297 (1995), pp. 1–28.
- [14] H. J. H. CLERCX AND C. H. BRUNEAU, *The normal and oblique collision of a dipole with a no-slip boundary*, Comput. Fluids, 35 (2006), pp. 245–279.
- [15] M. CHENG, J. LOU AND L. S. LUO, *Numerical study of a vortex ring impacting a flat wall*, J. Fluid Mech., 660 (2010), pp. 430–455.
- [16] L. D. COUCH AND P. S. KRUEGER, *Experimental investigation of vortex rings impinging on inclined surfaces*, Exp. Fluids, 51 (2011), pp. 1123–1138.
- [17] P. ORLANDI, *Vortex dipoles impinging on circular cylinders*, Phys. Fluids A, 5 (1993), pp. 2196–2206.
- [18] R. VERZICCO, J. B. FLOR, G. J. F. VAN HEIJST AND P. ORLANDI, *Numerical and experimental study of the interaction between a vortex dipole and a circular cylinder*, Exp. Fluids, 18 (1995), pp. 153–163.
- [19] J. J. ALLEN, Y. JOUANNE AND B. N. SHASHIKANTH, *Vortex interaction with a moving sphere*, J. Fluid Mech., 587 (2007), pp. 337–346.
- [20] P. J. F. DE SOUSA, *Three-dimensional instability on the interaction between a vortex and a stationary sphere*, Theor. Comput. Fluid Dyn., 26 (2012), pp. 391–399.
- [21] M. SREEDHAR AND S. RAGAB, *Large eddy simulation of longitudinal stationary vortices*, Phys. Fluids, 6 (1994), pp. 2501–2514.
- [22] J. R. MANSFIELD, O. M. KNIO AND C. MENEVEAU, *Dynamic LES of colliding vortex rings using a 3D vortex method*, J. Comput. Phys., 152 (1999), pp. 305–345.
- [23] T. T. LIM AND T. B. NICKELS, *Instability and reconnection in the head-on collision of two vortex rings*, Nature, 357 (1992), pp. 225–227.
- [24] J. M. FADDY AND D. I. PULLIN, *Flow structure in a model of aircraft trailing vortices*, Phys. Fluids, 17 (2005), 085106.
- [25] S. RAGAB AND M. SREEDHAR, *Numerical simulation of vortices with axial velocity deficits*, Phys. Fluids, 7 (1995), pp. 549–558.
- [26] L.-W. CHEN, C.-Y. XU AND X.-Y. LU, *Numerical investigation of the compressible flow past an aerofoil*, J. Fluid Mech., 643 (2010), pp. 97–126.
- [27] C.-Y. XU, L.-W. CHEN AND X.-Y. LU, *Large eddy simulation of the compressible flow past a wavy cylinder*, J. Fluid Mech., 665 (2010), pp. 238–273.
- [28] X.-Y. LU, S.-W. WANG, H.-G. SUNG, S.-Y. HSIEH AND V. YANG, *Large-eddy simulations of turbulent swirling flows injected into a dump chamber*, J. Fluid Mech., 527 (2005), pp. 171–195.
- [29] L.-W. CHEN, G.-L. WANG AND X.-Y. LU, *Numerical investigation of a jet from a blunt body opposing a supersonic flow*, J. Fluid Mech., 684 (2011), pp. 85–110.
- [30] K. SHARIF, R. VERZICCO AND P. ORLANDI, *A numerical study of three-dimensional vortex ring instabilities: viscous corrections and early nonlinear stage*, J. Fluid Mech., 279 (1994), pp. 351–375.
- [31] P. G. SAFFMAN, *The number of waves on unstable vortex rings*, J. Fluid Mech., 84 (1978), pp. 625–639.
- [32] P. J. ARCHER, T. G. THOMAS AND G. N. COLEMAN, *Direct numerical simulation of vortex ring evolution from the laminar to the early turbulent regime*, J. Fluid Mech., 598 (2008), pp. 201–226.
- [33] M. BERGDORF, P. KOUMOUTSAKOS AND A. LEONARD, *Direct numerical simulation of vortex*

- rings at $Re_{\Gamma} = 7500$* , J. Fluid Mech., 581 (2007), pp. 495–505.
- [34] P. J. ARCHER, T. G. THOMAS AND G. N. COLEMAN, *The instability of a vortex ring impinging on a free surface*, J. Fluid Mech., 642 (2010), pp. 79–94.
- [35] J. JEONG AND F. HUSSAIN, *On the identification of a vortex*, J. Fluid Mech., 285 (1995), pp. 69–94.
- [36] T. MAXWORTHY, *The structure and stability of vortex rings*, J. Fluid Mech., 51 (1972), pp. 15–32.
- [37] S. KRISHNAMOORTHY AND J. S. MARSHALL, *Three-dimensional blade-vortex interaction in the strong vortex regime*, Phys. Fluids, 10 (1998), pp. 2828–2845.
- [38] A. A. GOSSLER AND J. S. MARSHALL, *Simulation of normal vortex-cylinder interaction in a viscous fluid*, J. Fluid Mech., 431 (2001), pp. 371–405.
- [39] J. Z. WU, H. Y. MA AND M. D. ZHOU, *Vorticity and Vortex Dynamics*, Springer, 2006.